Direct imaging of individual organic molecules in supramolecular assembly strongly fixed via multivalent electrostatic interactions

Ikumi Akita, Yohei Ishida, Tetsu Yonezawa**

Division of Materials Science and Engineering, Faculty of Engineering, Hokkaido University, Kita 13 Nishi 8, Kita-ku, Sapporo, Hokkaido 060-8628, Japan.

*ishida-yohei@eng.hokudai.ac.jp, tetsu@eng.hokudai.ac.jp

ABSTRACT: Recent developments in electron microscopy and novel techniques for the precise control of low-dimensional substrate materials have led to the emergence of direct imaging of organic molecules. However, supramolecular assemblies constructed via non-covalent interactions are structurally unstable under electron bean irradiation. This study focused on a supramolecular assembly of well-isolated organic molecules based on multivalent electrostatic interactions, where anionically charged clay mineral nanosheets were used as a host material. Direct imaging of the single organic molecules and supramolecular assemblies on the monolayer clay mineral nanosheets was achieved via annular dark field scanning transmission electron microscopy using heavy metal atom markers. The versatility of multivalent electrostatic interactions for the stable fixation of organic molecules during electron microscopic imaging was demonstrated. This

strategy can be applied to a wide range of supramolecular systems comprising various guest molecules and host materials, thereby broadening the scope of atomic-scale imaging.

INTRODUCTION

Improved electron microscopic equipment and techniques for the precise control of low-dimensional nanomaterials[1–4] have led to advancements in the direct observation of single organic molecules and their supramolecular assemblies. Electron microscopy, including aberration corrected transmission electron microscopy (TEM) and scanning TEM (STEM), is the only atomic-scale imaging technique that allows for direct observation of the local structure of individual molecules with high spatio-temporal resolution.[5,6] Instead, conventional characterization methods for organic materials, such as optical spectroscopy and X-ray techniques, provide statistically averaged data based on a large number of molecules.

The isolation of organic molecules has been a key aspect of stable TEM and STEM research during the last two decades, where the much smaller secondary electron scattering cross-sections of these molecules result in less damage.[5–7] Electron beam damage is an issue particularly for the study of beam sensitive organic molecules and their assemblies and are typically suppressed using low acceleration voltages or low electron-dose conditions.[8–11] Macroscopic supporting materials are required for fixation and isolation of the target molecules during stable TEM and STEM observation, as they prevent dropout, migration, and aggregation. The supporting material and target molecule should be distinguishable with a large contrast, where nanocarbon materials (e.g., graphene, carbon nanotubes, and fullerene) are the most commonly used supporting substrate. Several methods have been developed for the fixation of molecules to nanocarbon substrates, including encapsulation into graphene layers, carbon nanotubes, or fullerene, direct attachment via

covalent bonding, and weak adsorption via non-covalent interactions (e.g., van der Waals or π-π interactions).[5,6,12–14] High-resolution TEM (HRTEM) can be used to visualize an entire molecular framework,[5,7] while high-angle annular dark field (ADF) STEM captures heavy metal atom markers (e.g., Pt,[13] Cu,[14] Ru,[15] and W[16]) coordinated within the molecule. These heavy metal atom markers exhibit bright contrast in ADF-STEM, which allows for visualization of single molecules on a host material with a more complex structure than graphene analogs with a single atom thickness. Organic molecules in supramolecular assemblies based on non-covalent interactions exhibit a flexible and non-periodic structure that is easily affected by the dropout, migration, or aggregation of the molecules under electron beam irradiation. Thus, TEM and STEM analysis of these organic molecules remains a challenge.

The use of anionic charged clay mineral nanosheets as a host material for a supramolecular assembly of well-isolated organic molecules has been investigated to prevent aggregation via multivalent electrostatic interactions.[17] These clay mineral nanosheets are a 2D nanomaterial with a thickness of *ca*. 1 nm, and can be obtained by exfoliating clay minerals, which is a layered aluminosilicate. There are many types of clay minerals, where the smectite group (e.g., saponite and montmorillonite) is widely used owing to its unique characteristics, including moderate anionic charge density, exfoliation to individual nanosheets (or stacking thereof) in aqueous solutions, and optical transparency of smaller exfoliated particles in visible light.[17–20] The general chemical formula of smectite is $[(Si_{8-x}Al_x)(Mg_{6-y}Al_y)O_{20}(OH)_4]\cdot(x-y)Y^+$, where Y represents the balancing cations that compensate for the anionic charge (Figure 1). A completely exfoliated clay mineral (i.e., monolayer) can thus be defined as a family of 2D nanosheets.

Stable atomic-scale imaging of monolayer clay mineral nanosheets via ADF-STEM was recently reported for the first time by the current authors.[21,22] The present study aimed to directly

image single organic molecules and supramolecular assemblies on monolayer clay mineral nanosheets using heavy metal atom markers. Electrostatic interactions are a weak non-covalent interaction, and enabled strong fixation of each organic molecule on the ionic 2D nanosheet supports. The local information obtained via electron microscopy using the proposed approach was complemented with averaged information from spectroscopic analysis to correlate the structural characteristics and properties or functionalities of individual molecular species during characterization.

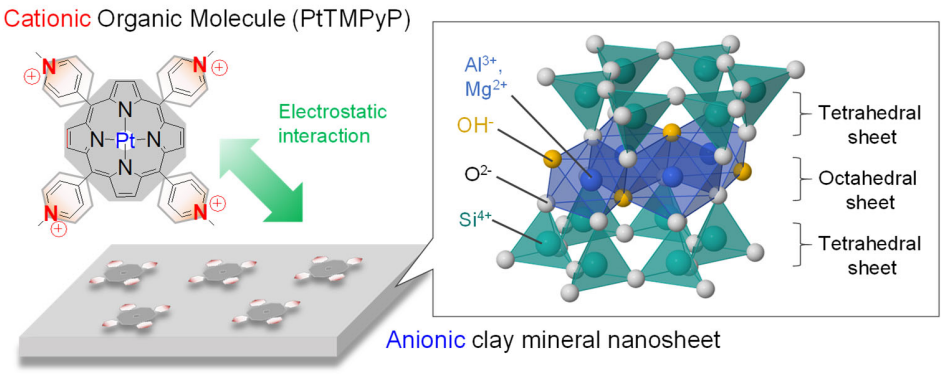

Figure 1. Schematic illustrations of a supramolecular assembly based on multivalent electrostatic interactions between the anionic clay mineral nanosheet and cationic organic molecule (PtTMPyP) (left), and the unit structure of the monolayer clay mineral nanosheet (montmorillonite) (right).

EXPERIMENTAL SECTION

Specimen preparation. Montmorillonite is a typical anionic clay mineral and was acquired from Kunimine Industries (Kunipia F). The chemical structure of montmorillonite corresponded to the formula $Na_{0.66}(Al_{3.34}Mg_{0.66})Si_8O_{20}(OH)_4$ with a cation exchange capacity (CEC) of 1.19 meq g^{-1}.

The montmorillonite was purified by preparing a raw clay dispersion (300 mL, 10 g L^{-1}) in centrifuge bottles, which was centrifuged at a rotation speed of 7000 rpm for 15 min. The supernatant was collected, poured into a container with 1500 mL ethanol, and mixed for 1 h at 70 °C. The resulting colloidal solution was filtered through a polytetrafluoroethylene (PTFE) membrane with a pore size of 0.1 μm (Millipore). The solids were collected and dried under vacuum in a rotary pump overnight. The dried solids were dispersed in ultrapure water and stored overnight for complete exfoliation into nanosheets. Pt(II) tetrakis(1-methylpyridinium-4-yl) porphyrin chloride (PtTMPyP; Frontier Scientific) was dissolved in ultrapure water. The water content of the clay and PtTMPyP was determined via thermogravimetry and differential thermal analysis (TG-DTA) using a thermogravimetry analyzer (TGA, Shimadzu DTG60H) before preparing the aqueous solutions.

Characterization. The PtTMPyP-clay assemblies were prepared by mixing the aqueous solutions of clay and PtTMPyP. The saturated concentration for monomer adsorption was determined based on the ultraviolet-visible (UV-vis) adsorption spectra on a series of samples with known loading levels of PtTMPyP vs. CEC of clay ranging from 10% to 160 (UV-1800; SHIMADZU). The STEM/TEM specimens were prepared by drop-casting the water dispersion of PtTMPyP-clay on a perforated carbon-coated Cu grid. STEM analysis was conducted using a JEM-ARM200F (JEOL) equipped with spherical aberration correctors at an acceleration voltage of 80 kV and camera length of 100 mm. The probe size was set to 8C with a condenser lens aperture of 30 μm (CL2) in size. The convergence semi-angle of the incident probe was 13.8 mrad, and the inner and outer detection semi-angles of the ADF detector were 54 and 220 mrad, respectively. Fourier transform was performed using the DigitalMicrograph (Gatan).

RESULTS AND DISCUSSION

Monomeric adsorption of cationic molecules on anionic clay mineral nanosheet via multivalent electrostatic interactions. The monomeric adsorption of PtTMPyP on the clay mineral nanosheets was confirmed using absorption spectroscopy, where the absorption spectra of the PtTMPyP aqueous solution (free molecules) and PtTMPyP-clay assembly dispersions are given in Figure 2a. The concentration of molecules on the clay mineral nanosheets was expressed as the loading level vs. the cation exchange capacity (CEC) of the clay, which is the ratio between the amount of cation charges of the molecule and the CEC of the clay mineral nanosheet. Specifically, a loading level of 100% vs. CEC of the clay indicated that the number of cationic sites in the guest adsorbed on the clay surface was the same as the number of anionic sites on the clay surface. The maximum absorption wavelengths of the Soret band were 401 nm for the free molecules and 422 nm for the molecules adsorbed on the sheet. This shift to the longer wavelengths upon adsorption on the sheet was attributed to planarization of the methylpyridinium substituents with respect to the porphyrin core.[23] The Lambert–Beer plot of the absorbance at 401 and 422 nm against the loading level exhibited linearity at concentrations below 90%, indicating monomeric adsorption on the clay mineral nanosheet (Figure 2b). At concentrations above 90%, the spectra can be expressed based spectral fitting of two components for free PtTMPyP (λ_{max} = 401 nm) and adsorbed PtTMPyP on clay (λ_{max} = 422). Therefore, the excess PtTMPyP was in the bulk solution and did not undergo further deposition or aggregation on the clay mineral nanosheets. Accordingly, ADF-STEM samples were prepared at a saturated adsorption concentration of 90% (PtTMPyP90%-clay) as the optimal condition.

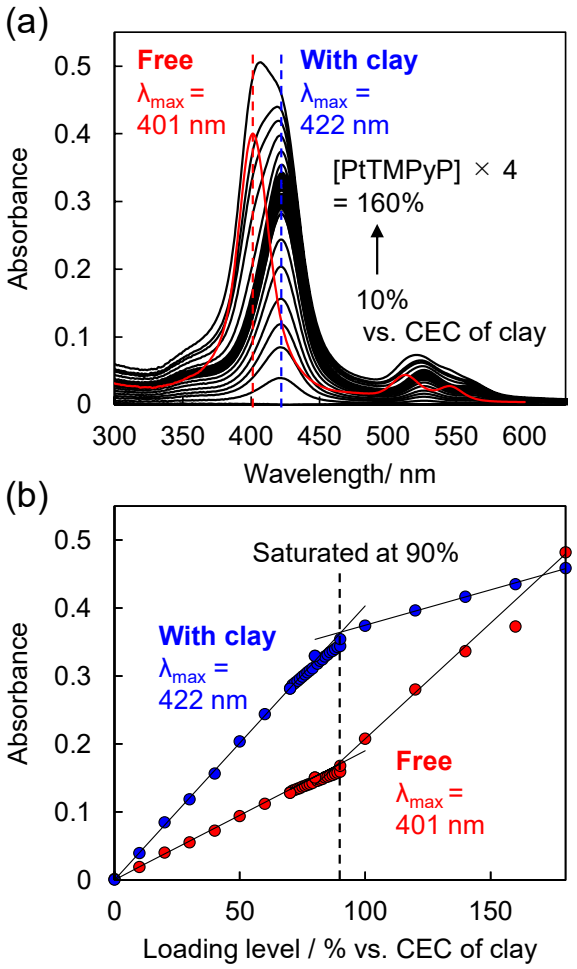

Figure 2. Spectral characterization of PtTMPyP-clay dispersion in water. (a) Absorption spectra of PtTMPyP-clay assemblies at various molecule loading levels up to 160% vs. CEC of clay in aqueous solution, where the maximum absorption wavelength of PtTMPyP in water (free) and adsorbed on clay mineral nanosheet (with clay) are 401 (red) and 422 nm (blue), respectively. (b) Lambert-Beer plots obtained from the absorption spectra at 401 (red) and 422 nm (blue).

ADF−STEM observation of PtTMPyP-clay mineral nanosheet assemblies. ADF−STEM images of the PtTMPyP90%-clay assemblies were acquired at low and medium magnification corresponding to the pixel size of 0.25×0.25 and 0.04×0.04 nm^2 per pixel, respectively (Figure 3). The monolayer region was determined from the contrast difference in the low magnification observations (Figure 3a),[24] while uniform distribution of the Pt markers on the entire nanosheet surface was observed at medium magnification, where no segregation to the edge or interior of the sheets occurred (Figures 3b and c). The contrast and the number of Pt atoms increased as the number of layers was increased from one (1L) to three (3L). In addition to the bright contrast of the Pt atoms, the clay mineral nanosheets were observed stably and exhibited the characteristic periodic hexagonal contrast pattern of pristine clay mineral nanosheets.[21,22] These observations demonstrated that Pt atoms are a valid marker for ADF−STEM imaging of guest molecules assembled on a clay mineral nanosheet, as well as on simpler substrates such as graphene.[13–15] The Fourier transform (Figure 3d) corresponding to the medium magnification ADF-STEM image of the monolayer region (Figure 3c) revealed that the in-plane distance was similar to previously reported values for the (*hk*0) facet of montmorillonite.[25] This was confirmed in all observations, indicating that the crystal structure of the nanosheets remained intact after monomeric adsorption of PtTMPyP on the clay nanosheet substrates via multivalent electrostatic interaction.

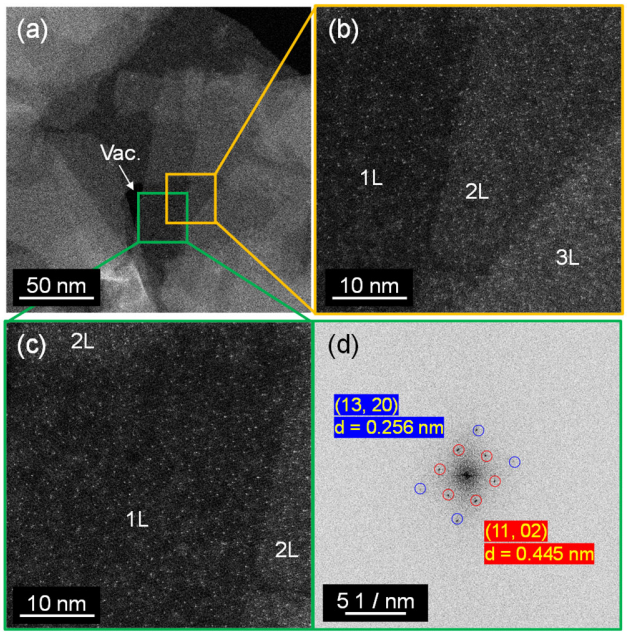

Figure 3. ADF−STEM images of PtTMPyP90%-clay at various magnifications. (a) Layer number from one (1L) to three (3L) was determined at low magnification (1024×1024 pixels, 0.25×0.25 nm^2/pixel, 20 μs/pixel). (b, c) Uniform dispersion of the Pt marker on monolayer clay mineral nanosheet of the green and orange regions at medium magnification (1024×1024 pixels, 0.04×0.04 nm^2/pixel, 20 μs/pixel). (d) Corresponding Fourier transform of the green area in inverted color.

ADF−STEM images of PtTMPyP90%-clay were acquired at pixel time of 10, 15, and 20 μs at high magnification (1024×1024 pixels, 0.013×0.013 nm^2/pixel). Only the images acquired during the first scan have been discussed further to avoid including artifacts caused by the degradation of the clay mineral nanosheets by repeated scanning. The image focus was optimized in an additional region near the target region. The first scans in different fields of view are given in Figures 4a to c. The Pt atom markers were observed stably, and no aggregation, migration, or dropout occurred, even at the atomic scale. A pixel time longer than 15 μs was optimal for

distinguishing the periodical contrast of the clay mineral nanosheet and bright contrast of Pt atoms without significant streaking.

The local loading level of PtTMPyP-clay was determined by dividing the area of the monolayer region by the number of Pt atoms in each field of view, as denoted in Figures 4a to c and Figure S1. The average loading level over the 16 fields of view was 87.5 ± 4.8%, which was in good agreement with the optimal preparation ratio of 90% determined by absorption spectroscopy (Figure 2). The occupied areas and corresponding ADF-STEM images are given in Table S1 and Figure S1. To the best of our knowledge, this is the first successful atomic-scale observation of a molecular assembly constructed via weak non-covalent interactions, where the observations corresponded well with the averaged spectroscopic data.

The direct observations were used to determine the individual intermolecular distances and relative conformations, which is not possible in conventional spectroscopic analyses. The histogram of the nearest-neighbor distance of each bright spot (i.e., the intermolecular distance of PtTMPyP) was shown in Figure S2a. The average intermolecular distance on the ADF-STEM projection of Figure 3c was 0.90 nm, which is much shorter than the diameter of the PtTMPyP molecule of 1.26 nm and the intermolecular distance of 1.65 nm assuming a uniform arrangement of the bright spots on the projection (Figure S2b and c). The diameter of PtTMPyP was determined as 1.26 nm using the semi-empirical molecular orbital method, where the cross-sectional area of the molecule was assumed to be circular.[26] Note that the existence of aggregation cannot be determined from only the intermolecular distance since three-dimensional information (i.e., 3D structure through the sheet) is compressed into 2D image on the ADF-STEM projection. The three-dimensional relative configuration of the molecules was, therefore, sorted into three groups by considering the number of neighboring bright spots as well as the intermolecular distance (Figure

4d). Circles with a diameter of 1.26 nm were superimposed onto the center of the Pt atoms in the ADF−STEM image of PtTMPyP90%-clay acquired at a pixel time of 20 μs, where the circles were shaded blue, yellow or red depending on the state of the molecule (Figure 4d). The blue circles indicated a completely isolated molecule, where the distance from the nearest Pt marker was larger than 1.26 nm. The yellow circles indicated that the molecules were isolated as monomers when observed from the front and back through the clay mineral nanosheet, but the distance from the nearest Pt marker was less than 1.26 nm. Most of the Pt markers were assigned to this group. The red circles indicated Pt markers that could not be interpreted as monomers, as they occurred in a region in which three molecules overlapped. This migration was attributed to electron beam irradiation, and untangling did not occur during further scanning. The subsequent ADF-STEM images of PtTMPyP90%-clay are given in Figure S3. No obvious changes in the number and relative conformation of the Pt markers was observed during four times of repeated scanning, while the clay mineral nanosheets were gradually damaged with each scan. Note that dozens scans disrupted the relative conformation of the isolated Pt markers as the clay mineral nanosheet decomposed, but no significant desorption or aggregation of the markers was observed (Figure S4). The Pt markers exhibited excellent stability during ADF−STEM analysis compared to specimens prepared via simple physisorption. Specimens based on conventional substrates typically exhibit a low barrier for migration that allows for significant molecular motions on a shorter time scale than image capture.[6,27–29] Furthermore, Pt atoms physisorbed on clay mineral nanosheets, which were prepared by sputtering deposition, showed less stability during ADF−STEM observation (Figure S5). These unexpected results suggest strong fixation of PtTMPyP molecules via multivalent electrostatic interactions during the observation.

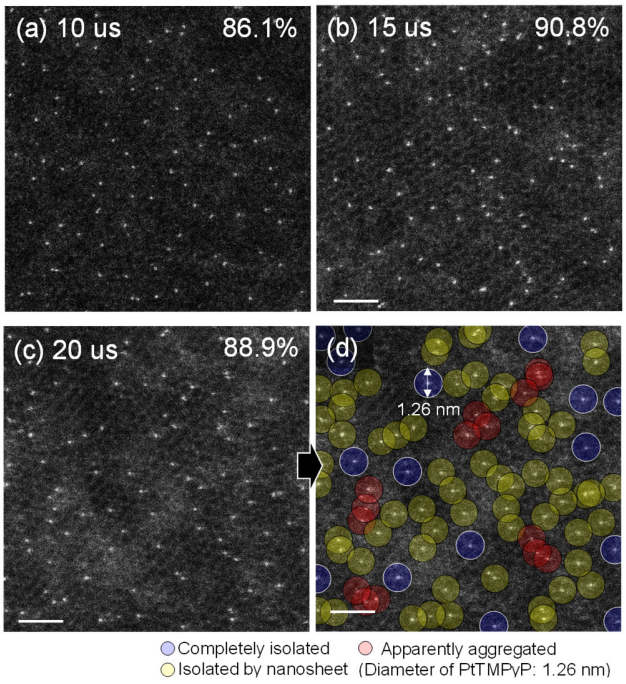

Figure 4. ADF−STEM images of PtTMPyP90%-clay acquired at high magnification at various pixel times. Images were acquired during the first scan in different fields of view, where pixel times included (a) 10, (b) 15, and (c) 20 μs (1024×1024 pixels, 0.013×0.013 nm^2/pixel). The percentages in each panel given the local loading level (area of the monolayer region divided by the number of Pt atoms). (d) Image acquired at a pixel time of 20 μs with the diameter of the PtTMPyP molecules (1.26 nm) superimposed onto the center of the Pt marker atoms. Scale bars = 2 nm.

It should be noted that hydrogen atoms are easily knocked on by electron beam irradiation, leading to cleavage of the C-H bonds and subsequent cross-linking between adjacent molecules during TEM and STEM analysis of molecular assemblies.[6,14] This cross-linking can lead to pseudo-stability of the heavy metal markers. Therefore, we confirmed that there was a low possibility of cross-linking at least between the molecules, since the completely independent molecules remained stable during several scans using specimens with a lower molecular density of 20% vs. CEC of clay to ensure a higher proportion of completely isolated PtTMPyP molecules (Figure 5). The overlaid circles shaded in the same manner as Figure 4d. However, the effect of molecular residues and the possibility of cross-linking between molecules and sheets cannot be discussed from this experiment, and thus further investigation is needed in this regard

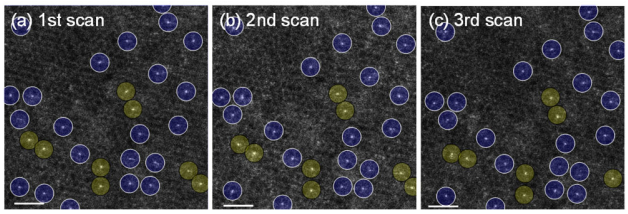

Figure 5. Stability of Pt markers during sequential ADF–STEM scanning. Sequential ADF−STEM images of PtTMPyP20%-clay continuously acquired during the (a) first, (b) second, and (c) third scans (1024×1024 pixels, ×15M, 0.013×0.013 nm^2/pixel, 20 μs/pixel), where the Pt markers were classified as either completely isolated (blue) or isolated by the clay mineral nanosheet (yellow) based on the diameter of PtTMPyP (1.26 nm). Dwell time of the image was 20.9 s. Scale bars = 2 nm.

Estimation of Coulombic attraction energy for multivlent electrostatic interaction. The fixation of the molecules via multivalent electrostatic interactions in this system was evaluated based on the Coulombic attraction energy (V) as follows:

$$V = \alpha \frac{1}{r} \quad (1)$$

$$\alpha = \frac{1}{4\pi\varepsilon\varepsilon_0} q_1 q_2 N_A \ (const) \qquad (2)$$

where r is the point-charge distance, ε is the relative permittivity, ε_0 is the permittivity of free space, q is the amount of charge, and N_A is the Avogadro constant. Determining the relative permittivity of the medium between the molecules and clay mineral nanosheets was challenging. Instead, an ε value of 1 was used during the calculations because moisture was mostly removed from the system during vacuum drying at 65 °C, and previously reported ε values of atomically thin two-dimensional materials are close to 1.[30–32] Assuming that a PtTMPyP molecule adsorbs on a monolayer clay mineral nanosheet, the Coulombic attraction energy (V_n; n = 1, 2, 3, or 4) between the four cationic charges of methylpyridinium substituents in PtTMPyP and the nearest four anionic charges of the clay surface were calculated. The Coulombic attraction energy of multivalent electrostatic interactions (V_{MEI}) was determined as follows:

$$V_{MEI} = V_1 + V_2 + V_3 + V_4$$

$$= \alpha \left(\frac{1}{r_1} + \frac{1}{r_2} + \frac{1}{r_3} + \frac{1}{r_4}\right) = \alpha \sum_{n=1}^{4} \frac{1}{r_n} \quad (3)$$

The variable anion-cation distance (r_n) was determined based on several assumptions. The CEC (1.19 meq g^{-1}) and specific surface area (780 m^2 g^{-1}) of clay gives a surface anion charge density of 0.943 e^- nm^{-2}. Thus, assuming a hexagonal array, the distance between the anion charges in the

plane direction was 1.11 nm. The intramolecular distance between the cationic charges of PtTMPyP was calculated as 1.05 nm.[33] Further, assuming that the anion and cation charges were localized at the octahedral layer of the clay mineral nanosheet and at the nitrogen atom of the methylpyridinium substituent in PtTMPyP, the *z* height between the cation and anion charges was 7.4 Å. The *z* height of PtTMPyP on the clay mineral nanosheets was based on a dihedral angle between the porphyrin core and methylpyridinium substituents of 43°, which was chosen based on a previous report on structural minimization of metal-free TMPyP adsorbed on clay mineral nanosheets.[33] Consequently, the maximum and minimum Coulombic attraction energy per molecule under vacuum (STEM atmosphere) was calculated as 173 and 154 kcal mol^{-1} via the least-square method for variable *r*. The arrangements of PtTMPyP on clay mineral nanosheets corresponding to the maximum and minimum total Coulombic attraction energy are shown in Figure 6. Further, the anion-cation distance and Coulombic attraction energy between each of the four cation charges in a molecule and the nearest anion charge in the clay mineral nanosheets are given in Table S2. The high charge density of the clay mineral nanosheet sled to minimal location dependence of V_{MEI} (*ca*. 20 kcal in the above calculations). Thus, the molecules at all locations on the nanosheet are under a uniform influence of the Coulombic interactions. The order of magnitude of the maximum and minimum total Coulombic attraction energies was comparable to the dissociation energy of covalent bonds such as C–C and C=C bonds (83.65 and 146.03 kcal mol^{-1}, respectively). This was much larger than the dissociation energy of π−π or CH−π non-covalent interactions in graphemic materials (11.95 kcal mol^{-1})[28] or the maximum adsorption energy of Pt atoms on graphene is *ca*. 33 kcal mol^{-1} by DFT calculations.[34] The stable observation of molecular assemblies during ADF−STEM analysis was thus attributed to strong fixation via multivalent electrostatic interactions. This estimation is based on many assumptions. For example, repulsion

between neighboring molecules was ignored because the repulsive forces parallel to the *xy*-plane with the surrounding molecules cancel one another under very dense conditions, as was the case in 90% CEC adsorption.

The strong multivalent interaction and the dense charge of the nanosheets allowed the strong fixation of the adsorbed molecules at the initial location of adsorption, thereby preventing rearrangement on the surface. This result is in good agreement with a previous report that multi-cationic molecules strongly adsorb on the clay mineral nanosheet surface, and do not desorb in an aqueous dispersion.[20,35] The local adsorption density of the PtTMPyP20%-clay specimen varied widely from 0% to 55.5% due to mixing of the clay and molecule dispersions (Figure S6).[35] This phenomenon also led to the deviation of intermolecular distance in PtTMPyP90%-clay (Figure 4).

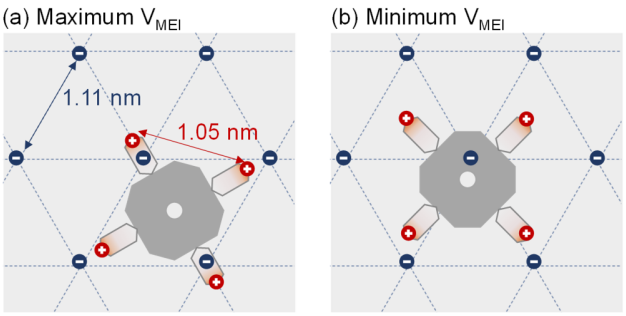

Figure 6. Schematic arrangement of PtTMPyP on clay mineral nanosheet. Arrangements at the (a) maximum and (b) minimum total Coulombic attraction energy of multivalent electrostatic interaction (V_{MEI}), where the average distance between the anion charges is 1.11 nm and the intramolecular distance between the cation charges of PtTMPyP is 1.05 nm.

CONCLUSION

In conclusion, strong fixation of organic molecules via multivalent electrostatic interactions enabled stable imaging of individual organic molecules in a supramolecular assembly on two-dimensional clay mineral nanosheets via electron microscopy. This approach facilitated visualization of the conformation of the individual molecules and assembly. Stable TEM and STEM imaging of organic molecules and supramolecular structures constructed via non- covalent interactions are crucial in the advancement of electron microscopic techniques. Common graphene-support based systems have limitations due to the small energy required to stabilize target molecules, but this strategy can be applied to a wide range of supramolecular systems consisting of various guest molecules and host materials. This approach is expected to widen the scope of atomic-scale imaging of organic molecules and assemblies.

ASSOCIATED CONTENT

Supporting Information. The supporting information is available free of charge via the Internet at http://pubs.acs.org. Table of loading level determined from ADF−STEM analysis, additional ADF−STEM images, subsequential ADF−STEMimages, and table for the value of Coulombic attraction energy are included (PDF).

AUTHOR INFORMATION

Corresponding Authors

* Yohei Ishida − Division of Materials Science and Engineering, Faculty of Engineering, Hokkaido University, Kita 13 Nishi 8, Kita-ku, Sap-poro, Hokkaido 060-8628, Japan; ORCID 0000-0001-8541-2714; E-mail: ishida-yohei@eng.hokudai.ac.jp

* Tetsu Yonezawa − Division of Materials Science and Engineering, Faculty of Engineering, Hokkaido University, Kita 13 Nishi 8, Kita-ku, Sap-poro, Hokkaido 060-8628, Japan; ORCID 0000-0001-7371-204; E-mail: tetsu@eng.hokudai.ac.jp

Author

Ikumi Akita − Division of Materials Science and Engineering, Faculty of Engineering, Hokkaido University, Kita 13 Nishi 8, Kita-ku, Sap-poro, Hokkaido 060-8628, Japan; ORCID 0000-0002-5843-4050

Author Contributions

Y.I. conceived and designed the project. Y.I. and I.A. performed all experiments and analyses. T.Y. supervised the project. I.A. wrote the manuscript using the input provided by the other authors.

Notes

The authors declare no competing interests.

ACKNOWLEDGMENT

This work was supported by a Grant-in-Aid for JSPS Fellows DC1 (grant number 18J20894) from the Japan Society for the Promotion of Science to I. A. Y.I. acknowledges financial support from JSPS KAKENHI grant number 18K14070, Japan Prize Foundation, the Asahi Glass Foundation, the JFE 21st Century Foundation, and the Foundation for Interaction in Science & Technology. Partial financial support by the Cooperative Research Program of "Network Joint Research Center for Materials and Devices" (20201248, 20191100, and 20191201 to T.Y.), Japan, are gratefully acknowledged.

REFERENCES

(1) Tan, C.; Cao, X.; Wu, X. J.; He, Q.; Yang, J.; Zhang, X.; Chen, J.; Zhao, W.; Han, S.; Nam, G. H.; et al. Recent Advances in Ultrathin Two-Dimensional Nanomaterials. *Chem. Rev.* **2017**, *117*, 6225–6331.

(2) Büchner, C.; Heyde, M. Two-Dimensional Silica Opens New Perspectives. *Prog. Surf. Sci.* **2017**, *92*, 341–374.

(3) Lin, Y. C.; Susi, T.; Kotakoski, J.; Ramasse, Q. M.; Kepaptsoglou, D.; Meyer, J. C.; Suenaga, K. Towards Atomically Precise Manipulation of 2D Nanostructures in the Electron Microscope. *2D Mater.* **2017**, *4*, 042004.

(4) Sohlberg, K.; Pennycook, T. J.; Zhou, W.; Pennycook, S. J. Insights into the Physical Chemistry of Materials from Advances in HAADF-STEM. *Phys. Chem. Chem. Phys.* **2015**, *17*, 3982–4006.

(5) Nakamura, E. Atomic-Resolution Transmission Electron Microscopic Movies for Study of Organic Molecules, Assemblies, and Reactions: The First 10 Years of Development. *Acc. Chem. Res.* **2017**, *50*, 1281–1292.

(6) Skowron, S. T.; Chamberlain, T. W.; Biskupek, J.; Kaiser, U.; Besley, E.; Khlobystov, A. N. Chemical Reactions of Molecules Promoted and Simultaneously Imaged by the Electron Beam in Transmission Electron Microscopy. *Acc. Chem. Res.* **2017**, *50*, 1797–1807.

(7) Koshino, M.; Tanaka, T.; Solin, N.; Suenaga, K.; Isobe, H.; Nakamura, E. Imaging of Single Organic Molecules in Motion. *Science* **2007**, *316*, 853–853.

(8) Chen, Q.; Dwyer, C.; Sheng, G.; Zhu, C.; Li, X.; Zheng, C.; Zhu, Y. Imaging Beam-Sensitive Materials by Electron Microscopy. *Adv. Mater.* **2020**, *32*, 1–42.

(9) Krivanek, O. L.; Dellby, N.; Murfitt, M. F.; Chisholm, M. F.; Pennycook, T. J.; Suenaga, K.; Nicolosi, V. Gentle STEM: ADF Imaging and EELS at Low Primary Energies. *Ultramicroscopy* **2010**, *110*, 935–945.

(10) Sasaki, T.; Sawada, H.; Hosokawa, F.; Sato, Y.; Suenaga, K. Aberration-Corrected STEM/TEM Imaging at 15kV. *Ultramicroscopy* **2014**, *145*, 50–55.

(11) Susi, T.; Meyer, J. C.; Kotakoski, J. Quantifying Transmission Electron Microscopy Irradiation Effects Using Two-Dimensional Materials. *Nat. Rev. Phys.* **2019**, *1*, 397–405.

(12) Skowron, S. T.; Roberts, S. L.; Khlobystov, A. N.; Besley, E. The Effects of Encapsulation on Damage to Molecules by Electron Radiation. *Micron* **2019**, *120*, 96–103.

(13) Gerkman, M. A.; Sinha, S.; Warner, J. H.; Han, G. G. D. Direct Imaging of Photoswitching Molecular Conformations Using Individual Metal Atom Markers. *ACS Nano* **2019**, *13*, 87–96.

(14) Mittelberger, A.; Kramberger, C.; Meyer, J. C. Insights into Radiation Damage from Atomic Resolution Scanning Transmission Electron Microscopy Imaging of Mono-Layer $CuPcCl_{16}$ Films on Graphene. *Sci. Rep.* **2018**, *8*, 4813.

(15) Koshiya, S.; Yamashita, S.; Kimoto, K. Microscopic Observation of Dye Molecules for Solar Cells on a Titania Surface. *Sci. Rep.* **2016**, *6*, 2–7.

(16) Kengmana, E. S.; Lee, J. K.; Li, X.; Warner, J. H.; Han, G. G. D. Self-Assembly of Bowlic Supramolecules on Graphene Imaged at the Individual Molecular Level Using Heavy Atom Tagging. *Small* **2020**, 2002860.

(17) Ishida, Y. Manipulation of Supramolecular 2D Assembly of Functional Dyes toward Artificial Light-Harvesting Systems. *Pure Appl. Chem.* **2015**, *87*, 3–14.

(18) Takagi, S.; Eguchi, M.; Tryk, D. A.; Inoue, H. Porphyrin Photochemistry in Inorganic/Organic Hybrid Materials: Clays, Layered Semiconductors, Nanotubes, and Mesoporous Materials. *J. Photochem. Photobiol. C Photochem. Rev.* **2006**, *7*, 104–126.

(19) Okada, T.; Ide, Y.; Ogawa, M. Organic-Inorganic Hybrids Based on Ultrathin Oxide Layers: Designed Nanostructures for Molecular Recognition. *Chem. Asian J.* **2012**, *7*, 1980–1992.

(20) Bujdák, J. Effect of the Layer Charge of Clay Minerals on Optical Properties of Organic Dyes. A Review. *Appl. Clay Sci.* **2006**, *34*, 58–73.

(21) Akita, I.; Ishida, Y.; Yonezawa, T. Atomic-Scale Imaging of a Free-Standing Monolayer Clay Mineral Nanosheet Using Scanning Transmission Electron Microscopy. *J. Phys. Chem. Lett.* **2020**, *11*, 3357–3361.

(22) Akita, I.; Ishida, Y.; Yonezawa, T. Distinctive Stability of Free-Standing Monolayer Clay Mineral Nanosheet under Transmission Electron Microscopy. *Phys. Chem. Chem. Phys.* **2020**, *22*, 25095–25102.

(23) Ishida, Y.; Masui, D.; Shimada, T.; Tachibana, H.; Inoue, H.; Takagi, S. The Mechanism of the Porphyrin Spectral Shift on Inorganic Nanosheets: The Molecular Flattening Induced by the Strong Host-Guest Interaction Due to the "Size-Matching Rule." *J. Phys. Chem. C* **2012**, *116*, 7879–7885.

(24) Akita, I.; Ishida, Y.; Yonezawa, T. Counting the Layer Number of Free-Standing Montmorillonite Nanosheets Using Annular Dark Field Scanning Transmission Electron Microscopy. *Clay Sci.* **2019**, *23*, 41–45.

(25) *The X-Ray Identification and Crystal Structures of Clay Minerals*; Brown, G., Ed.; Mineralogical Society, Clay Minerals Group: London, 1961.

(26) Stewart, J. J. P. Comparison of the Accuracy of Semiempirical and Some DFT Methods for Predicting Heats of Formation. *J. Mol. Model.* **2004**, *10*, 6–12.

(27) Colliex, C.; Gloter, A.; March, K.; Mory, C.; Stéphan, O.; Suenaga, K.; Tencé, M. Capturing the Signature of Single Atoms with the Tiny Probe of a STEM. *Ultramicroscopy* **2012**, *123*, 80–89.

(28) Georgakilas, V.; Tiwari, J. N.; Kemp, K. C.; Perman, J. A.; Bourlinos, A. B.; Kim, K. S.; Zboril, R. Noncovalent Functionalization of Graphene and Graphene Oxide for Energy Materials, Biosensing, Catalytic, and Biomedical Applications. *Chem. Rev.* **2016**, *116*, 5464–5519.

(29) Daukiya, L.; Seibel, J.; De Feyter, S. Chemical Modification of 2D Materials Using Molecules and Assemblies of Molecules. *Adv. Phys. X* **2019**, *4*, 1625723.

(30) Hüser, F.; Olsen, T.; Thygesen, K. S. How Dielectric Screening in Two-Dimensional Crystals Affects the Convergence of Excited-State Calculations: Monolayer MoS_2. *Phys. Rev. B* **2013**, *88*, 245309.

(31) Laturia, A.; Van de Put, M. L.; Vandenberghe, W. G. Dielectric Properties of Hexagonal Boron Nitride and Transition Metal Dichalcogenides: From Monolayer to Bulk. *npj 2D Mater. Appl.* **2018**, *2*, 6.

(32) Mathew, K.; Sundararaman, R.; Letchworth-Weaver, K.; Arias, T. A.; Hennig, R. G. Implicit Solvation Model for Densityfunctional Study of Nanocrystal Surfaces and Reaction Pathways. *J. Chem. Phys.* **2014**, *140*, 084106.

(33) Ishida, Y.; Shimada, T.; Tachibana, H.; Inoue, H.; Takagi, S. Regulation of the Collisional Self-Quenching of Fluorescence in Clay/Porphyrin Complex by Strong Host-Guest Interaction. *J. Phys. Chem. A* **2012**, *116*, 12065–12072.

(34) Hasegawa, S.; Kunisada, Y.; Sakaguchi, N. Diffusion of a Single Platinum Atom on Light-Element-Doped Graphene. *J. Phys. Chem. C* **2017**, *121*, 17787–17795.

(35) Ishida, Y.; Masui, D.; Tachibana, H.; Inoue, H.; Shimada, T.; Takagi, S. Controlling the Microadsorption Structure of Porphyrin Dye Assembly on Clay Surfaces Using the "Size-Matching Rule" for Constructing an Efficient Energy Transfer System. *ACS Appl. Mater. Interfaces* **2012**, *4*, 811–816.

Table of Contents Graphic